

# Two-photon sideband transition in a driven quantum Rabi model : Quantitative discussions with derived longitudinal drives and beyond the rotating wave approximation

Byoung-moo Ann,<sup>\*</sup> Wouter Kessels, and Gary A. Steele

*Kavli Institute of Nanoscience, Delft University of Technology, 2628 CJ Delft, The Netherlands*

(Dated: August 3, 2021)

In this work, we analytically and numerically study the sideband transition dynamics of the driven quantum Rabi model (QRM). We focus in particular on the conditions when the external transverse drive fields induce first-order sideband transitions. Inducing sideband transitions between two different systems is an essential technique for various physical models, including the QRM. However, despite its importance, a precise analytical study has not been reported yet that successfully explains the sideband transition rates in a driven QRM applicable for all system parameter configurations. In our study, we analytically derive the sideband transition rates based on second-order perturbation theory, not relying on the rotating wave approximation (RWA) [1]. Our formulae are valid for all ranges of drive frequencies and system's parameters. Our analytical derived formula agrees well with the numerical results in a regime of moderate drive amplitudes. Interestingly, we have found a non-trivial longitudinal drive effect derived from the transverse drive Hamiltonian. This accounts for significant corrections to the sideband transition rates that are expected without considering the derived longitudinal effect. Using this approach, one can precisely estimate the sideband transition rates in the QRM not confining themselves within specific parameter regimes. This provides important contributions for understanding experiments described by the driven QRM.

## I. INTRODUCTION

The quantum Rabi model (QRM)[2] constitutes the essence of the light-matter interactions at the quantum level. It specifically describes the interaction between a two-level system (qubit) and a single cavity mode. The QRM has been extensively studied both for fundamental interest and for applications in quantum information processing. In addition, the QRM can describe many systems. It was originally formulated to mathematically describe cavity quantum electrodynamics (QED), and study the interaction between a trapped atom and cavity mode. Beyond atomic physics, it can also be extended to any other systems that have an analogy with the cavity-QED, such as quantum-dots in microcavities and various types of qubits that are transversely coupled to superconducting cavities. Moreover, the extended versions of the QRM have been widely investigated [3–5].

The question of how to implement in-situ tuneable state transfer between the qubit and cavity mode (sideband transitions) is an important aspect of studying the QRM. In particular, it is crucial for quantum gate operation using qubits and can be employed for quantum state engineering of the cavity. There are several ways to achieve this. One approach is to suddenly switch the transition frequency of the qubit ( $\omega_q$ ). If the qubit is initially far-off resonant from the cavity transition frequency ( $|\omega_q - \omega_c| \gg 1$ ), then we consider the qubit to be isolated and they are effectively uncoupled. However, if the qubit's transition frequency jumps from  $\omega_q$  to  $\omega_c$ , then the qubit and cavity become resonant and coherent state transfer begins. Consequently, by shifting the  $\omega_q$ , we can turn the interaction between the qubit and the cavity on and off. The other approach is to parametrically modulate the qubit's transition frequency.

Sideband transitions between the qubit and cavity occur when the modulation frequency  $\omega_m$  satisfies the matching conditions ( $\omega_m = |\omega_q \pm k\omega_c|$ ,  $k$  is integer).

These approaches require that the frequency of the qubit should be tunable over short time scales. This is technically feasible if one employs superconducting qubits with SQUID loops and on-chip magnetic flux lines. The sudden frequency switch was realized in [6], where the authors create Fock states in a superconducting cavity. Inducing the first-order sideband transitions by flux modulation was proposed in [7] and was experimentally implemented in [8].

In all cases, the systems can be modeled by the QRM. Although these cases successfully demonstrate the state transfer from the qubit to the cavity, introducing tuneability into the qubit's transition frequency leads to another side-effect: pure dephasing induced by external noise. For example, when the tuneability relies on the magnetic flux through the squid loops, then the magnetic field noise into the loops accounts for the qubit's pure dephasing.

One can also induce the sideband transitions without any frequency tuneability of the qubit and cavity by applying the external transverse drive at the proper frequencies. This scheme is implementable with a fixed frequency qubit. Therefore, the system is insensitive to the external noise and the qubit's dephasing rate is only limited by the qubit's decay rate [9]. For the first-order sideband transition in the QRM, which is typically the most attractive type, the transition is unfortunately dipole forbidden and therefore only a two (or any higher even number) photon drive can induce the transition. This complicates the analytical solution for the transition rates because we cannot capture the transitions simply by first-order perturbation theory.

In this paper, we perform a quantitative study of the first-order sideband transition in the QRM induced by two-photon transverse drive fields. We analytically derive the transition rates based on perturbative calculation up-to second order without relying on the rotating wave approximations in the Hamiltonian. We specifically investigate the parameter regimes that are familiar in circuit quantum electrodynamics (QED) experiments. In circuit QED, the frequency matching condition for sideband transitions often requires drive parameters that are beyond the rotating wave approximation (RWA) [10], and therefore one should not rely on the RWA in the analytical derivation of the transition rates. Moreover, under the transverse drive field, the qubit's frequency should be modulating at the lab frame, which effectively amounts to the longitudinal drive. This effect was typically neglected although it also can induce the sideband transitions.

Whereas a number of studies have examined how the external transverse drive fields affect the qubits or similar systems beyond the RWA [11–15], and there are a few studies have quantitatively discuss the sideband transition rates between the qubits and cavities [10, 16–20], a satisfactory quantitative study beyond the RWA regime and considering the derived longitudinal drive effect has not yet been reported. To our best knowledge, the initial attempt to analytically derive the two-photon sideband transition rates in the QRM was given in [16]. In that study, a charge qubit device dispersively coupled to the cavity was modeled by the QRM. However, the analytically derived transition rates are a factor of four smaller than the simulation results. In our work, we found that the RWA significantly distorts the calculated sideband transition rates for some system parameters. We also investigate if the transverse drive field accounts for a derived longitudinal drive effect, which also significantly contributes to the total sideband transition rates. Our analytical predictions of the frequency matching conditions and sideband transition rates are well consistent with the numerical results when we have moderate drive amplitudes. Although our analytical model fails to explain the sideband transition rates as the drive strength becomes comparable to the detuning between the qubit and drive, it nonetheless yields more precise predictions than the model relying on the RWA.

This paper is organized as follows. In Sec. II, we analytically derive the expected matching frequencies and sideband transition rates based on the perturbation theory up to second-order. A description of the numerical simulation performed in this study is given in Sec. A 2. We compare the analytical and numerical calculation results in Sec. III with extensive parameter scanning. We also discuss the validity and limitation of our theory in this section. Finally, we conclude our paper in Sec. IV.

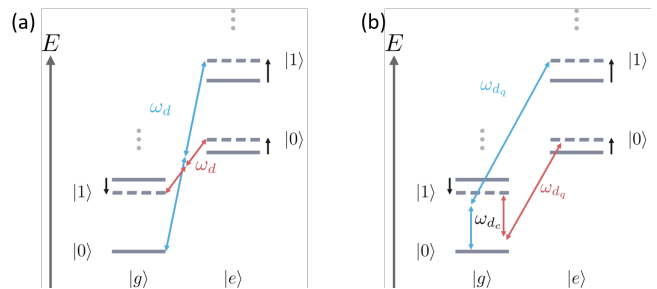


FIG. 1. Descriptions of the first order red and blue sideband transitions in quantum Rabi model (QRM). The arrows indicate the external drives that satisfy the matching conditions for red and blue sideband transitions (red and blue arrow, respectively). A two-photon drive is required because the first order sideband transitions in QRM are dipole forbidden. (a) Single frequency (monochromatic) drive. (b) Two-frequency (bi-chromatic) drive.  $|gn\rangle$  and  $|en\rangle$  (corresponding to dashed lines) represent the dressed states of the system. The black arrows indicate the frequency shifts induced by the external drive fields and the qubit-cavity bare coupling  $g$ . The bare states are depicted by solid lines.

## II. THEORETICAL DESCRIPTION

In this section, we derive an analytical formula to predict the matching frequencies and sideband transition rates. We investigate two possible schemes for the first order two-photon sideband transitions in the QRM, as shown in Fig. 1. The possible scheme for the first order sideband transitions is described in Fig. 1(a), where the drive field has only a single frequency component  $\omega_d$  (monochromatic drive). The downside of this approach is that there is no flexibility in choosing the drive frequency for the given qubit and resonator frequencies. When using two different drive frequencies (i.e., a bi-chromatic drive), we can have more flexibility in choosing the drive frequencies. Fig. 1(b) describes the bi-chromatic drive case. One drive frequency is close to the resonator ( $\omega_{dc}$ , which is called a resonator friendly drive in this paper), and the other is close to the qubit ( $\omega_{dq}$ , qubit friendly). The solid line and dashed lines refer to the bare and dressed energy states of the QRM, respectively.

### A. Schrieffer-Wolff transformation

The transversely driven QRM Hamiltonian reads,

$$\hat{H} = \underbrace{\frac{\omega_q}{2}\hat{\sigma}_z + \omega_c\hat{a}^\dagger\hat{a} + g(\hat{a}^\dagger + \hat{a})\hat{\sigma}_x}_{\hat{H}_{\text{QRM}}} + \underbrace{\sum_i \Omega_d^{(i)}\hat{\sigma}_x \cos(\omega_d^{(i)}t)}_{\hat{H}_{\text{drive}}}. \quad (1)$$

Here,  $\hat{\sigma}_{z,x}$  is the z and x components of the Pauli operators, and  $\hat{a}$  is the cavity field operator.  $\omega_{q,c}$  are angular

frequencies of the qubit and cavity, respectively.  $\Omega_d^{(i)}$  and  $\omega_d^{(i)}$  refer to  $i$ -th component of the drive amplitude and frequency. It is also useful to define  $\epsilon_d^{(i)} = \Omega_d^{(i)}/2$  the drive strength for use later in this paper. We are interested in the dispersive coupling regime where  $|\omega_q - \omega_c| \gg g$ . We are also interested in those drive frequencies  $\omega_d^{(i)}$  that are far off resonant to  $\omega_{q,c}$ , and those drive amplitudes  $\Omega_d^{(i)}$  that are smaller than  $|\omega_{q,c} - \omega_d|$ . With these parameter conditions,  $\hat{H}_d$  can be considered as a perturbation to  $\hat{H}_{\text{QRM}}$ . We can then approximately diagonalize the  $\hat{H} = \hat{H}_{\text{QRM}} + \hat{H}_{\text{drive}}$  using Schrieffer-Wolff transformation [21]. The transform operator  $\hat{U}$  takes a form of  $\hat{U} = \exp(\beta^* \hat{\sigma}_+ - \beta \hat{\sigma}_-)$ . We define  $\hat{X} = \beta \hat{\sigma}_- - \beta^* \hat{\sigma}_+$  in the following. The transformed Hamiltonian  $\hat{H}'$  is given

by,

$$\hat{H}' = \hat{U} \hat{H} \hat{U}^\dagger + i(\partial_t \hat{U}) \hat{U}^\dagger. \quad (2)$$

The first term in Eq. 2 can be calculated using the Hausdorff expansion [ref],

$$e^{\lambda \hat{X}} \hat{H} e^{-\lambda \hat{X}} = \hat{H} - \lambda [\hat{H}, \hat{X}] + \frac{\lambda^2}{2} [[\hat{H}, \hat{X}], \hat{X}] + \dots \quad (3)$$

When  $\beta \ll 1$ , we can truncate the expansion to the low order of  $\lambda$ . To capture the two-photon transitions, we should include at least to the second order of  $\lambda$ . Meanwhile, the second term in Eq. 2 can be approximated by [ref],

$$(i\partial_t \hat{U}) \hat{U}^\dagger \approx \frac{i}{2} (\beta^* \dot{\beta} - \beta \dot{\beta}^*) \hat{\sigma}_z + i(\dot{\beta} \hat{\sigma}_- - \dot{\beta}^* \hat{\sigma}_+). \quad (4)$$

$\hat{H}'$  is then expressed by,

$$\begin{aligned} \hat{H}' \approx & \underbrace{\frac{\omega_q}{2} \hat{\sigma}_z + \omega_c \hat{a}^\dagger \hat{a} + g(\hat{a} + \hat{a}^\dagger) \hat{\sigma}_x}_{\hat{H}_{\text{QRM}}} + \underbrace{\sum_i \Omega_d^{(i)} \hat{\sigma}_x \cos(\omega_d^{(i)} t)}_{\hat{H}_{\text{drive}}} \underbrace{-\omega_q(\beta^* \hat{\sigma}_+ + \beta \hat{\sigma}_-) - i(\dot{\beta} \hat{\sigma}_- - \dot{\beta}^* \hat{\sigma}_+)}_{\hat{H}_1} \\ & + \underbrace{\sum_i \Omega_d^{(i)} \cos(\omega_d^{(i)} t) (\beta^* + \beta) \hat{\sigma}_z - \omega_q |\beta|^2 \hat{\sigma}_z - i \frac{1}{2} (\beta^* \dot{\beta} - \beta \dot{\beta}^*) \hat{\sigma}_z}_{\hat{H}_z} \\ & - \underbrace{g(|\beta|^2 + \beta^*) \hat{a}^\dagger \hat{\sigma}_+ - g(|\beta|^2 + \beta) \hat{a} \hat{\sigma}_- - g(|\beta|^2 + \beta^*) \hat{a} \hat{\sigma}_+ - g(|\beta|^2 + \beta) \hat{a}^\dagger \hat{\sigma}_-}_{\hat{H}_{sb}} \\ & + \underbrace{g(\beta^* + \beta) (\hat{a} + \hat{a}^\dagger) \hat{\sigma}_z}_{\hat{H}_2} - \underbrace{\sum_i \Omega_d^{(i)} \cos(\omega_d^{(i)} t) \beta^* (\beta^* + \beta) \hat{\sigma}_+ - \sum_i \Omega_d^{(i)} \cos(\omega_d^{(i)} t) \beta (\beta^* + \beta) \hat{\sigma}_-}_{\hat{H}_3}. \end{aligned} \quad (5)$$

The main purpose of the transformation  $\hat{U}$  is to eliminate the  $\hat{H}_{\text{drive}}$ , the largest off-diagonal element in  $\hat{H}'$ . We need to chose proper  $\beta$  such  $\hat{H}_{\text{drive}} + \hat{H}_1 = 0$ .  $\hat{H}_z$  accounts for the qubit's frequency shifts and modulations.  $\hat{H}_{sb}$  is related with the sideband transitions.  $\hat{H}_2$  is derived longitudinal coupling between the qubit and cavity.  $\hat{H}_3$  is derived transverse drive. Both  $\hat{H}_2$  and  $\hat{H}_3$  are irrelevant to the sideband transition rates. We neglect the third and higher order terms of  $\beta$  in the derivation.

For time-periodical transverse drive,  $\beta$  typically takes a form of  $\sum_i \xi_i e^{i\omega_d^{(i)} t} + \sum_i \zeta_i e^{-i\omega_d^{(i)} t}$ , and here  $\xi_i$  and  $\zeta_i$  are time-independent values that we need to find to diagonalize the Hamiltonian. Consequently, we can always find the terms corresponding to the qubit's frequency modulation in  $\hat{H}_z$ . It is intriguing to point out that we obtain the longitudinal drive effect although we start with only the transverse drive fields. We call this derived longitudinal

drive in this paper. The effect of these derived frequency modulation in sideband transition rates was neglected in many previous works [10, 16–20]. In this study, however, we will prove that these effects significantly contribute to the sideband transition rates.

## B. Monochromatic drive

In this case, we have a drive Hamiltonian  $\hat{H}_{\text{drive}} = 2\epsilon_d \cos(\omega_d t) \hat{\sigma}_x$ . For this, the proper  $\beta$  is given by,

$$\beta = \frac{\epsilon_d}{\Delta} e^{i\omega_d t} + \frac{\epsilon_d}{\Sigma} e^{-i\omega_d t}. \quad (6)$$

Here,  $\Delta$  and  $\Sigma$  are  $\omega_q - \omega_d$  and  $\omega_q + \omega_d$  respectively. With this  $\beta$ ,  $\hat{H}_{\text{drive}} + \hat{H}_1 = 0$  satisfies. For  $\hat{H}_z$ , we obtain,

$$\hat{H}_z = \hat{\sigma}_z \times \left[ \left( \frac{\epsilon_d^2}{\Delta} + \frac{\epsilon_d^2}{\Sigma} \right) (1 + 2 \cos(2\omega_d t)) - \frac{2\omega_q \epsilon_d^2}{\Delta \Sigma} \cos(2\omega_d t) \right], \quad (7)$$

which explains the qubit frequency shifts  $\delta\omega_q$  and modulation with an amplitude  $\Omega_m = 2\epsilon_m$ , as given below.

$$\begin{aligned} \delta\omega_q &\approx 2 \frac{\epsilon_d^2}{\Delta} + 2 \frac{\epsilon_d^2}{\Sigma}, \\ \epsilon_m &\approx 2 \frac{\epsilon_d^2}{\Delta} + 2 \frac{\epsilon_d^2}{\Sigma} - \frac{2\omega_q \epsilon_d^2}{\Delta \Sigma}. \end{aligned} \quad (8)$$

The matching frequency can be found by considering  $\delta\omega_q$  and the dispersive shift  $\pm\chi$  in the qubit and cavity induced by the bare coupling  $g$ . We can approximate  $\chi$  by  $g^2/\Delta_{qc} + g^2/\Sigma_{qc}$ , where  $\Delta_{qc} = \omega_q - \omega_c$  and  $\Sigma_{qc} = \omega_q + \omega_c$ . Then, the matching conditions for blue and red sideband transitions are given by,

$$\begin{aligned} 2\omega_d &= \omega_q + \delta\omega_q + \omega_c + 2\chi \quad (\text{blue sideband}), \\ 2\omega_d &= |\omega_q + \delta\omega_q - \omega_c + 2\chi| \quad (\text{red sideband}). \end{aligned} \quad (9)$$

Eq. 9 is close-form expression of  $\omega_d$  because it exists in both the left-hand and right-hand sides.

When  $\omega_d$  satisfies each blue and red sideband condition, then the  $\hat{H}_{sb}$  at the qubit and cavity rotating frame is reduced to,

$$\begin{aligned} \hat{H}_{sb} &= \\ &\underbrace{-g \left( \frac{\epsilon_d^2}{\Delta^2} + \frac{2\epsilon_d^2}{\Delta \Sigma} \right) \hat{a}^\dagger \hat{\sigma}_+ + \text{h.c.}}_{\Omega_{sb}^{(0)}/2} \quad (\text{blue sideband}). \\ &-g \left( \frac{\epsilon_d^2}{\Delta^2} + \frac{2\epsilon_d^2}{\Delta \Sigma} \right) \hat{a}^\dagger \hat{\sigma}_- + \text{h.c.} \quad (\text{red sideband, } \omega_q > \omega_c). \\ &\underbrace{-g \left( \frac{\epsilon_d^2}{\Sigma^2} + \frac{2\epsilon_d^2}{\Delta \Sigma} \right) \hat{a}^\dagger \hat{\sigma}_- + \text{h.c.}}_{\Omega_{sb}^{(0)}/2} \quad (\text{red sideband, } \omega_q < \omega_c). \end{aligned} \quad (10)$$

We define  $\Omega_{sb}^{(0)}$  by the transition rates corresponding to the coefficients in front of the operators in Eq. 10. In addition to  $\Omega_{sb}^{(0)}$ , there is additional contribution to the sideband transition rates resulting from the qubit's frequency modulation at  $2\omega_d$  in Eq. 9. If  $\omega_d$  satisfies the two-photon sideband transitions, then  $2\omega_d$  also automatically satisfies the condition for the first order sideband transitions for both blue and red sideband transitions. This phenomena is analogous to inducing the first order sideband transition by modulating the flux through the squid loop of the frequency tunable qubits, which was first demonstrated in [8]. We define this contribution  $\Omega_{sb}^{(1)}$ , which amounts to  $2gJ_1(2\epsilon_m/\Delta_{qc})$ , where  $J_n(x)$  is the first kind of Bessel function of order  $n$ . The detail derivation is given in [8]. Finally, we can define  $\Omega_{sb} = \Omega_{sb}^{(0)} + \Omega_{sb}^{(1)}$  as the analytically predicted sideband transition rates.

### C. Bi-chromatic drive

Now, we consider the drive Hamiltonian given by  $\hat{H}_{\text{drive}} = 2\epsilon_{dq} \cos(\omega_{dq}t) \hat{\sigma}_x + 2\epsilon_{dc} \cos(\omega_{dc}t) \hat{\sigma}_x$ . The subscription  $dq$  and  $dc$  refer to qubit friendly and cavity friendly drives, as depicted in Fig. 1. In this case, we chose  $\beta$ , as below,

$$\beta = \frac{\epsilon_{dq}}{\Delta_1} e^{i\omega_{dq}t} + \frac{\epsilon_{dq}}{\Sigma_1} e^{-i\omega_{dq}t} + \frac{\epsilon_{dc}}{\Delta_2} e^{-i\omega_{dc}t} + \frac{\epsilon_{dc}}{\Sigma_2} e^{i\omega_{dc}t}. \quad (11)$$

Here,  $\Delta_1, \Delta_2 = \omega_q - \omega_{dq,dc}$  and  $\Sigma_1, \Sigma_2 = \omega_q + \omega_{dq,dc}$ , respectively. The drive induces the frequency shifts  $\delta\omega_q$ , as given in Eq. 12. It also modulates the qubit frequency with angular speeds of  $\omega_{dq} - \omega_{dc}$  and  $\omega_{dq} + \omega_{dc}$ . The amplitude of this modulation  $\epsilon_m$  is also given in Eq. 12.

$$\begin{aligned} \delta\omega_q &\approx 2 \frac{\epsilon_{dq}^2}{\Delta_1} + 2 \frac{\epsilon_{dq}^2}{\Sigma_1} + 2 \frac{\epsilon_{dc}^2}{\Delta_2} + 2 \frac{\epsilon_{dc}^2}{\Sigma_2}, \\ \epsilon_m &\approx \epsilon_{dq} \epsilon_{dc} \left[ \frac{1}{\Delta_1} + \frac{1}{\Delta_2} + \frac{1}{\Sigma_1} + \frac{1}{\Sigma_2} \right]. \end{aligned} \quad (12)$$

Then, the matching conditions are given by,

$$\begin{aligned} \omega_{dq} + \omega_{dc} &= \omega_q + \delta\omega_q + \omega_c + 2\chi \quad (\text{blue sideband}), \\ |\omega_{dq} - \omega_{dc}| &= |\omega_q + \delta\omega_q - \omega_c + 2\chi| \quad (\text{red sideband}). \end{aligned} \quad (13)$$

Eq. 13 is also close-form expression of  $\omega_{dq}$  and  $\omega_{dc}$ .

As in Sec. II B, we reduce  $\hat{H}_{sb}$  as below when the above frequency matching condition satisfy.

$$\begin{aligned} \hat{H}_{sb} &= \\ &\underbrace{-g \left( \frac{2\epsilon_{dq}\epsilon_{dc}}{\Delta_1\Delta_2} + \frac{\epsilon_{dq}\epsilon_{dc}}{\Delta_1\Sigma_2} + \frac{\epsilon_{dq}\epsilon_{dc}}{\Delta_2\Sigma_1} \right) \hat{a}^\dagger \hat{\sigma}_+ + \text{h.c.}}_{\Omega_{sb}^{(0)}/2} \quad (\text{blue sideband}). \\ &-g \left( \frac{\epsilon_{dq}\epsilon_{dc}}{\Delta_1\Delta_2} + \frac{\epsilon_{dq}\epsilon_{dc}}{\Delta_2\Sigma_1} + \frac{\epsilon_{dq}\epsilon_{dc}}{\Sigma_1\Sigma_2} \right) \hat{a}^\dagger \hat{\sigma}_- + \text{h.c.} \quad (\text{red sideband, } \omega_q > \omega_c). \\ &\underbrace{-g \left( \frac{\epsilon_{dq}\epsilon_{dc}}{\Delta_1\Delta_2} + \frac{\epsilon_{dq}\epsilon_{dc}}{\Delta_1\Sigma_2} + \frac{\epsilon_{dq}\epsilon_{dc}}{\Sigma_1\Sigma_2} \right) \hat{a}^\dagger \hat{\sigma}_- + \text{h.c.}}_{\Omega_{sb}^{(0)}/2} \quad (\text{red sideband, } \omega_q < \omega_c). \end{aligned} \quad (14)$$

From the above Eq. 14, we can obtain  $\Omega_{sb}^{(0)}$ . We should also consider the effect from  $\epsilon_m$  as in Sec. II B.  $\Omega_{sb}^{(1)}$  in this case takes the same expression as in the monochromatic drive case,  $\Omega_{sb}^{(1)} = 2gJ_1(2\epsilon_m/\Delta_{qc})$ . The analytically predicted sideband transition rate is then given by  $\Omega_{sb}^{(0)} + \Omega_{sb}^{(1)}$ .

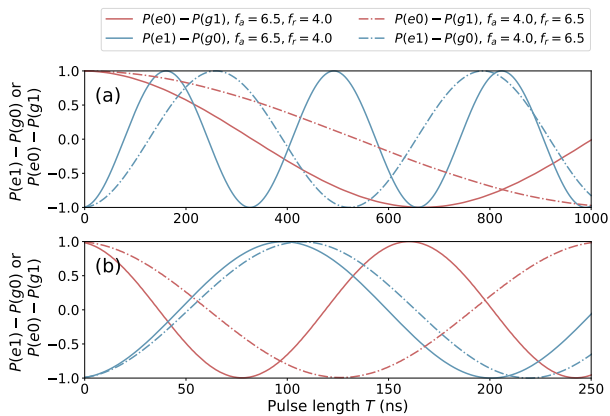


FIG. 2. The first order two-photon sideband transitions in the QRM with various system configurations. Eight different cases are present. The red and blue lines indicate the red and blue sideband transitions, respectively. (a) The sideband transitions by the monochromatic drive fields. (b) The sideband transitions by bi-chromatic drive fields. Please see the text and legend for further detail of the conditions in the numerical simulation.

#### D. Rotating wave approximation

Under the rotating wave approximation (RWA),  $\hat{H}_{\text{drive}}$  is approximated to,

$$\hat{H}_{\text{drive}}^{(\text{RWA})} \approx \sum_i \frac{\Omega_d^{(i)}}{2} (\hat{\sigma}_+ e^{-i\omega_d^{(i)} t} + \hat{\sigma}_- e^{i\omega_d^{(i)} t}). \quad (15)$$

This amounts to taking  $\Sigma_i \rightarrow \infty$ . The RWA model converges to the full model when we have  $\Sigma_i \gg \Delta_i$ . Here we define,  $\Delta_i = \omega_q - \omega_d^{(i)}$  and  $\Sigma_i = \omega_q + \omega_d^{(i)}$ . However, this condition often breakdowns with circuit QED device parameters [refs]. In Sec. III, we compare the analytical calculations based on both full and RWA models. We confirm that the calculations based on the full model show substantially better agreements to the numerical simulation. More detailed discussions will be provided there.

When taking the RWA in this work, we apply the approximation only to the drive Hamiltonian  $\hat{H}_d$ . Dropping energy non-conservative terms in the interaction part of the QRM is also considered as the RWA. In this case, the QRM is reduced to a Jynes-Cummings (JC) Hamiltonian. However, this yields to a too loose approximation. For example, we cannot capture blue sideband transition rate when using JC Hamiltonian. Therefore, we always keep the energy non-conservative interaction terms of the QRM in this work.

### III. BENCHMARKING WITH NUMERICAL SIMULATIONS

#### A. Overview

To verify the validity of the derived formula, we perform the numerical simulation with several system parameter sets. We define the drive and transition frequencies of the qubit and cavity as  $f_d = \omega_d/2\pi$ ,  $f_q = \omega_q/2\pi$ , and  $f_c = \omega_c/2\pi$ , respectively. In the bi-chromatic drive case, we define the qubit and resonator drive frequencies as  $f_{dq} = \omega_{dq}/2\pi$  and  $f_{dc} = \omega_{dc}/2\pi$ , respectively. For the QRM parameters, we investigate two cases here:  $f_{q,c} = 6.5, 4.0$  GHz and  $f_{q,c} = 4.0, 6.5$  GHz.

In the numerical simulation, we solve the time-dependent master equation of the driven QRM, and we get the time evolution of the qubit and cavity. For monochromatic drive cases, we sweep the  $f_d$  until the resonant sideband transition takes place to find the matching frequencies. The procedure is somewhat complicated for bi-chromatic drive cases. First, we fix  $f_{dc}$  by  $f_c - 500$  MHz. We parameterize the  $\epsilon_{dq}/2\pi$  and  $\epsilon_{dc}/2\pi$  with a real positive parameter  $\eta$ . Both are given by  $\epsilon_{dq}/2\pi = \eta \cdot 25$  MHz and  $\epsilon_{dc}/2\pi = \eta \cdot 317$  MHz, respectively. With these conditions, we sweep the  $f_{dq}$  until the resonant sideband transition takes place. More detail of the procedure for the numerical simulation is given in Appendix A 2.

In Fig. 2, we present the simulated time domain dynamics when the two-photon sideband transitions take place.  $g/2\pi$  in both cases is fixed by 200 MHz. Fig. 2(a) shows the results under a monochromatic drive with  $\epsilon_d/2\pi = 300$  MHz. Fig. 2(b) shows the results under a bi-chromatic drive when  $\epsilon_{dq}/2\pi = 25$  MHz and  $\epsilon_{dc}/2\pi = 317$  MHz, respectively ( $\eta = 1$ ). The definitions of  $\epsilon_d$ ,  $\epsilon_{dq}$ , and  $\epsilon_{dc}$  are the same as in the previous section. We can also confirm that whether the qubit is red or blue detuned to the cavity results in different sideband transition rates. This is already predictable from the analytical formula derived in Sec. II.

#### B. Monochromatic drives

In this subsection, we deal with only the monochromatic drive cases. The parameters that we use for the simulations are  $f_{q,c} = 6.5, 4.0$  GHz in Fig. 3(a,b) and  $f_{q,c} = 4.0, 6.5$  GHz in Fig. 3(c,d).  $g/2\pi$  in both cases is fixed by 200 MHz. The lines in Fig. 3 show the the analytically calculated sideband transition rates. We first obtained the matching frequencies based on Eq. 9, and we use these values when calculating the sideband transition rates. When analytically calculating  $\Omega_{sb}$  here and in the following of this paper, we replace  $\omega_q$  in the formula with  $\omega_q + \delta\omega_q$  for higher accuracy.

In Fig. 3, the sideband transition rates calculated by the full analytical model (solid lines) excellently agree with all the numerical simulation results, whereas the other model fails to explain all parameter cases. Notice-

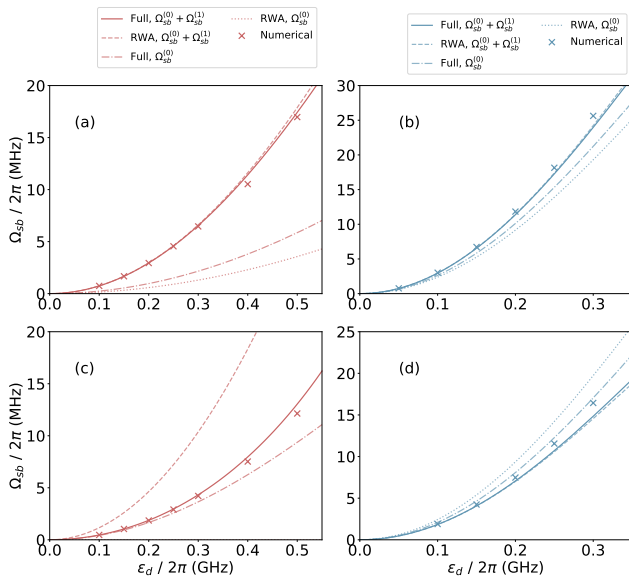


FIG. 3. Red and blue sideband transition rates ( $\Omega_{sb}$ ) induced by monochromatic drive fields. The lines indicate the analytically calculated sideband transition rates. See the legend for the detail information. The cross marks indicate the numerically simulated results based on the  $\hat{H} + \hat{H}_{drive}$ . (a,b)  $f_q = 6.5$  GHz and  $f_c = 4.0$  GHz. (c,d)  $f_q = 4.0$  GHz and  $f_c = 6.5$  GHz. In the case of (c), the fine dashed line (RWA,  $\Omega_{sb}^{(0)}$ ) in the legend) lies on x-axis, and thus hardly visible in the figure.

ably, the derived longitudinal drive ( $\Omega_{sb}^{(1)}$ ) significantly accounts for the total sideband transition rates. All these trends can be also found in the bi-chromatic drive cases in Sec. III C.

As  $\epsilon_d$  becomes larger, the accuracy of the analytical model decreases. This happens because the basic assumption for perturbative approach ( $\epsilon_d/|\omega_q - \omega_c| \ll 1$ ) in derivation of the analytical model becomes weakened. We can understand the large discrepancy in blue sideband cases in the same manner. The blue sideband transition requires the matching frequency  $f_d$  much closer to the  $f_q$  than the red sideband transition does. In Fig. 3(d), the numerical results with large drive strengths are more consistent with another analytical model (double-dashed line) rather than full model (solid line). This is an interesting coincidence to point out. The sideband transitions contributed by secondary longitudinal drive is significant in the red sideband cases but not in the blue sideband cases.

### C. Bi-chromatic drives

We investigate the bi-chromatic drive cases in this subsection.  $f_{q,c}$  and  $g$  used in the simulations are the same as in Sec. III B. We analytically find the proper  $f_{dq}$  based on the Eq. 12, fixing the  $f_{dc}$  to  $f_c - 500$  MHz.  $\epsilon_{dq}$  and  $\epsilon_{dc}$  are

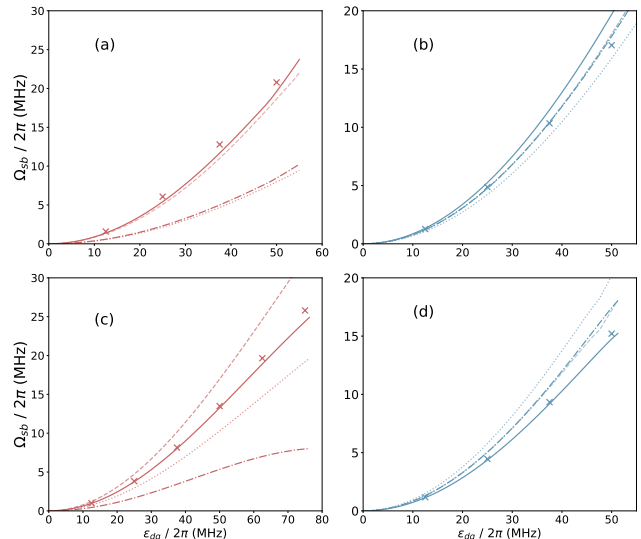


FIG. 4. Red and blue sideband transition rates  $\Omega_{sb}$  induced by bi-chromatic drive fields. The lines indicate the analytically calculated sideband transition rates. The cross marks indicate the numerically simulated results based on the  $\hat{H} + \hat{H}_{drive}$ . See the legend in Fig. 3 for more detailed information.  $\omega_{dc}$  is fixed by  $f_c - 500$  MHz.  $\epsilon_{dq}$  and  $\epsilon_{dc}$  are parameterized as described in Sec. A 2 (a,b)  $f_q = 6.5$  GHz,  $f_c = 4.0$  GHz. (c,d)  $f_q = 4.0$  GHz,  $f_c = 6.5$  GHz.

parameterized as described in Sec. A 2. We also analytically calculate the sideband transitions based on the results in Sec III A. Fig. 4 compares the sideband transition rates calculated by the numerical simulation (cross) and analytical calculation (line). The full analytical model (solid lines) explains the simulation results better than other models, except for the one case in Fig. 4(b). In the red sideband cases, we can clearly see the significant effect of the secondary longitudinal drive in the sideband transition rates ( $\Omega_{sb}^{(1)}$ ). This also results in approximately 15% correction to the total sideband transition rates in the blue sideband cases. The effect of the RWA is very conspicuous in Fig. 4(c) but not in other cases. In particular, we can hardly identify the effect of the RWA in Fig. 4(a).

### D. From strong to ultrastrong coupling regime

In the previous subsections, we have fixed  $g/2\pi$  by 200 MHz. In this subsection, we perform the simulation with different  $g$  while fixing the drive strengths and the other system parameters. We use  $f_q = 4.0$  GHz and  $f_c = 6.5$  GHz in the simulation. We scan  $g$  from 100 MHz (strong coupling regime) to 500 MHz (ultrastrong coupling regime).

In Fig. 5, we plot the red and blue sideband transition rates with different qubit-cavity coupling strength  $g$ . Fig. 5(a,b) describe mono-chromatic drive cases and

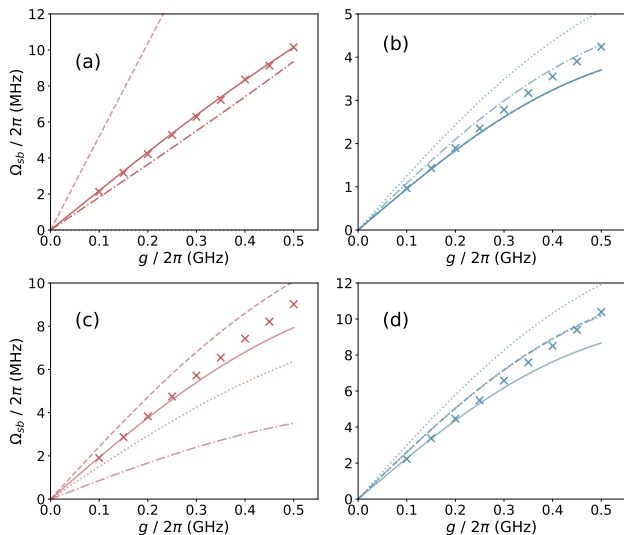


FIG. 5. Red and blue sideband transition rates  $\Omega_{sb}$  with different qubit—cavity coupling strength  $g$ . We fix  $f_q = 4.0$  GHz and  $f_c = 6.5$  GHz in the calculation. The lines indicate the analytically calculated sideband transition rates. The cross marks indicate the numerically simulated results based on the  $\hat{H} + \hat{H}_{drive}$ . See the legend in Fig. 3 for the detail information. (a,b) Monochromatic drive cases. Drive strength is fixed by  $\epsilon_d/2\pi = 100$  MHz. (c,d) Monochromatic drive cases. Drive strength is fixed by  $f_d$  is fixed by  $f_c - 500$  MHz. In all cases, we set  $\epsilon_{dq}/2\pi = 25$  MHz and  $\epsilon_{dc}/2\pi = 317$  MHz. In the case of (a), the fine dashed line (RWA,  $\Omega_{sb}^{(0)}$  in the legend) lies on x-axis, and thus hardly visible in the figure.

Fig. 5(c,d) describe bi-chromatic drive cases. Drive strengths  $\epsilon_d$  are fixed by 100 MHz (red) and 300 MHz (blue), respectively. Similar to the previous results in Fig. 3 and Fig. 4, the full analytical model (solid lines) explains the numerical simulation results better than the other model does when the drive strengths are small enough. As  $g$  becomes larger, the discrepancy between the numerical and analytical values also becomes larger. Eventually, the numerical results fall into the other analytical models in (b) and (d). We can also confirm that a significant portion of the  $\Omega_{sb}$  is attributed to  $\Omega_{sb}^{(1)}$ .

#### IV. CONCLUSION

In this paper, we have analytically and numerically studied the first order sideband transitions that are induced by two-photon drives in a quantum Rabi Hamiltonian. We confirm that the sideband transition rates can be accurately predicted based on the analytical formula when the parameters are in the perturbative regime ( $\epsilon_d/|\omega_q - \omega_d|$ ). We also confirm that the RWA significantly

misleads the prediction of the sideband transition rates for some system parameters. We also find that the transverse drive field can induce the secondary longitudinal drive Hamiltonian. In addition, we can confirm its significant contributions to total sideband transition rates. As the drive parameters deviate from the perturbative regime, we observe disagreement between numerical and analytical calculation, and consequently the other models coincidentally provide more accurate predictions. Our study significantly improves the accuracy of the analytical formula from the previous work.

#### ACKNOWLEDGMENTS

We acknowledge David Vitali for our helpful discussions. Byoung-moo Ann also acknowledges support from the European Union’s Horizon 2020 research and innovation program under the Marie Skłodowska-Curie grant agreement No. 722923 (OMT). This project also has received funding from the European Union’s Horizon 2020 research and innovation program under grant agreement No. 828826 - Quomorphic. The data that support the findings of this study are available in [22].

#### Appendix A: Method for numerical simulation

##### 1. General method

The dynamics of the system can be described by the equation,

$$d\hat{\rho}_{sys}/dt = -i[\hat{H}_{QRM} + \hat{H}_{drive}, \hat{\rho}_{sys}]. \quad (A1)$$

Here,  $\hat{\rho}_{sys}$  is a density matrix of the qubit and cavity. We do not take the dissipation into consideration. In the numerical study in this paper, we rigorously benchmark the real experiments. We set the rising and falling in the sideband drive strength as in the real experiments. Specifically,  $\epsilon_d(t)$  is defined as a pulse with 10-ns of Gaussian rising and falling time. We can then scan the pulse length and plot the quantum states of the system at the end of each pulses. We do not include the rising and falling times in the definition of the pulse length.

##### 2. Removing micro-oscillation

Fig. 6 provides a step-by-step description of our numerical simulation method. The simulation parameters used in Fig. 6 are  $\omega_q, \omega_c, \omega_d, \epsilon_d, g = 2\pi \times (6.5, 4.0, 0.1, 0.2, 5.278)$  GHz. The monochromatic drive frequency  $\omega_d$  satisfies the matching condition for the blue sideband transition. Fig. 6a shows the dynamics of the system under the sideband drive pulse with a length of 480 ns. Fig. 6(b) magnifies the area enclosed by the square in Fig. 6(a). One can identify the fast but small

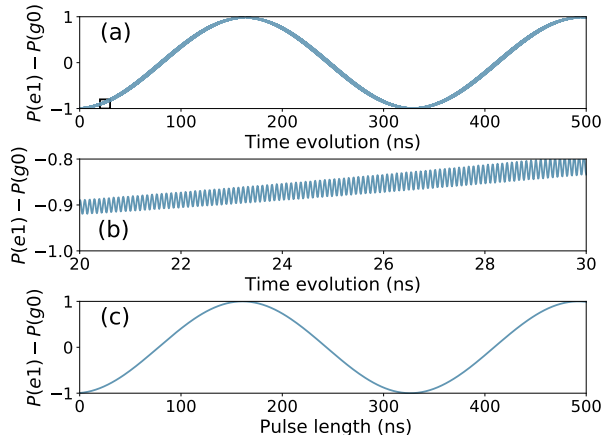


FIG. 6. Time-domain numerical simulation. (a) A direct solution of the master equation when the drive field satisfies the blue sideband transition. Please see the text for a description of the conditions in the simulation. We consider 10 ns Gaussian rising and falling time in the drive amplitude. (b) Zoom in on the black rectangular box in (a). We identify that the fast micro-oscillation and the frequency of this oscillation is the same as the drive frequency. (c) We plot the  $P(e1) - P(g0)$  at the end of the pulse with respect to the pulse length without rising and falling times. A clear sinusoidal oscillation is obtained.

oscillation in the quantum state of the system. This oscillation originates from the Hamiltonian's time dependence. We can remove the time dependence by moving to the rotating frame at  $\omega_d$ , and removing all the fast rotating components. This is what amounts to the rotating wave approximation (RWA). However, the RWA is only available when the  $\epsilon_d$  and  $|\omega_q - \omega_d|$  are small enough. These conditions are clearly not satisfied for the two-photon sideband transition with circuit QED parameters. We repeat the simulations by varying the pulse lengths, and we plot the states at the end of the pulses (when the pulse falling finishes). The result is given in Fig. 6(c). We obtain a clear sinusoidal curve without the fast oscillation.

The procedure described above is analogous with the real experiment. This explains why one still can see clear sinusoidal dynamics in the experiment, even with a very strong drive strength. We calculate  $P(e1) - P(g0)$  for the blue sideband transitions, and  $P(e0) - P(g1)$  for the red sideband transitions in this paper. Here,  $P$  refers to the probability to find the system in the states enclosed in the brackets. Once we obtain a sinusoidal oscillation from the

simulation, we then determine the sideband transition rate  $\Omega_{sb}$  from the period of the oscillation.

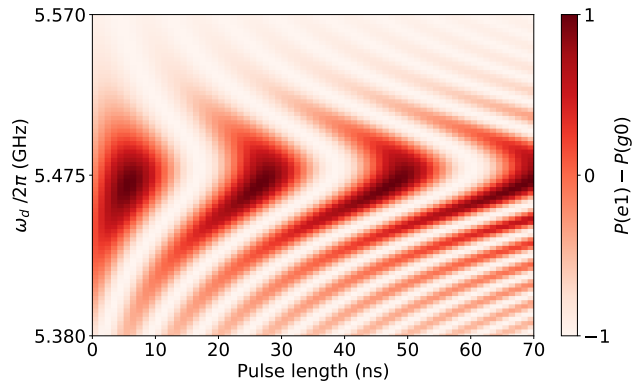


FIG. 7. Finding a matching frequency. This plot shows the dynamics of the two-state system (qubit) when we sweep the monochromatic drive frequency around the matching frequency that satisfies the resonant blue sideband transition. Please see the text for a description of the conditions that we used in the simulation.

### 3. Finding matching frequency

Fig. 7 describes how we found the matching frequencies for sideband transitions. All of the simulation parameters are the same in Fig. 6 except that  $\epsilon_d/2\pi$  is 500 MHz. We sweep  $\omega_d$  around the predicted matching frequency for blue sideband transition. In this case, the matching frequency is found at  $\omega_d/2\pi = 5.474$  GHz. The asymmetric shape is attributed to the fact that the frequency shift of qubit changes while sweeping the drive frequency.

### Appendix B: Extended data: Estimation of the matching frequencies

In this section, we present the analytically calculated matching frequencies compared to the numerical simulation results. All of the simulation conditions and parameters are the same in Fig. 3, Fig. 4, and Fig. ???. The lines in Fig. 8, Fig. 9, and Fig. 10 show the analytically calculated matching frequencies based on the formula that we obtained in Sec. II B. The matching frequencies obtained from the numerical simulation are denoted by cross marks. In general, the calculated matching frequencies based on the full drive Hamiltonian are in better agreement with the numerical results. The only the exception is Fig. 3(b). In this case, the numerical data deviates from the full analytical model due to the breakdown of the perturbative approach, and eventually gets closer to the RWA model coincidentally.

\* byoungmoo.ann@gmail.com

[1] I. I. Rabi *et al.* *Use of Rotating Coordinates in Magnetic Resonance Problems*, Rev. Mod. Phys. **26**, 167 (1954).



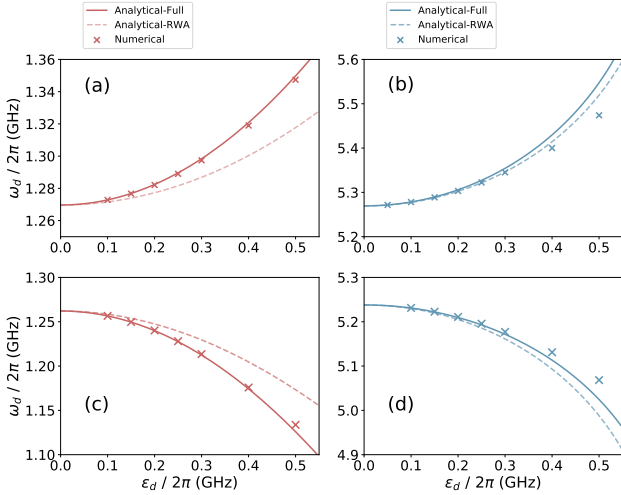


FIG. 8. Matching drive frequencies ( $\omega_d$ ) for two-photon red and blue sideband transitions induced by monochromatic drive fields. The single and double dashed lines indicate the analytically calculated matching frequencies the red and blue sideband transitions respectively. These are based on the full (single-dashed) and RWA model (double-dashed). The cross marks indicate the numerically simulated results based on the full model. (a,b)  $f_q = 6.5$  GHz and  $f_c = 4.0$  GHz. (c,d)  $f_q = 4.0$  GHz and  $f_c = 6.5$  GHz.

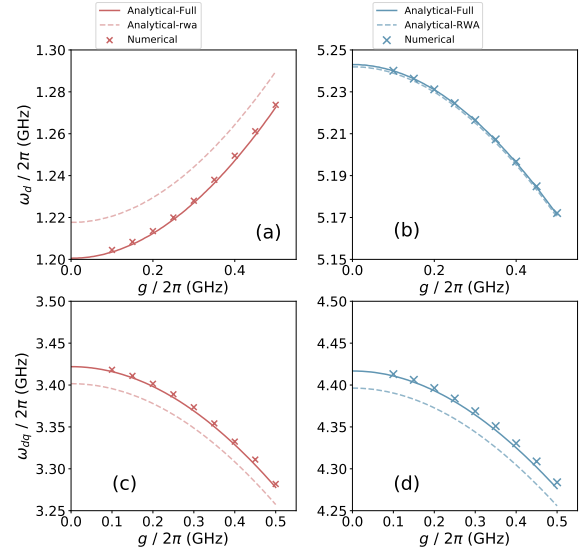


FIG. 10. The matching drive frequencies with different qubit and cavity bare coupling  $g$ .  $f_q = 4.0$  GHz and  $f_c = 6.5$  GHz in the calculation. (a,b) Mono-chromatic drive cases. Drive strength is fixed by  $\epsilon_d/2\pi = 100$  MHz. (c,d) Bi-chromatic drive cases.  $f_{dc}$  is fixed by  $f_c - 500$  MHz. In all cases, we set  $\epsilon_{dq}/2\pi = 25$  MHz and  $\epsilon_{dc}/2\pi = 317$  MHz.

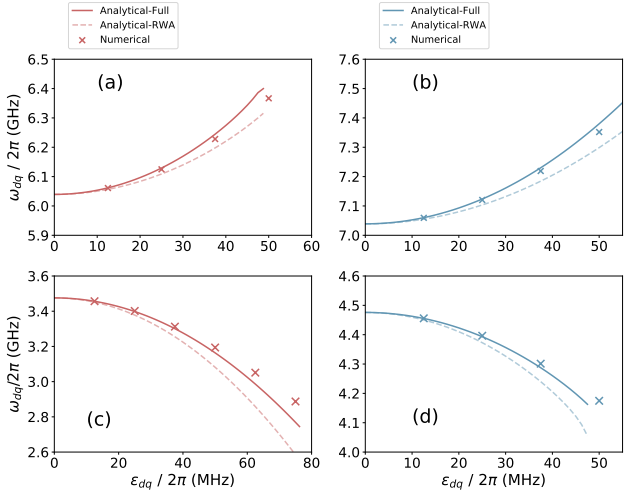


FIG. 9. Matching drive frequencies ( $\omega_{dq}$ ) for two-photon red and blue sideband transition induced by bi-chromatic drive fields when  $f_{dc}$  is fixed by  $f_c - 500$  MHz.  $\epsilon_{dq}$  and  $\epsilon_{dc}$  are parameterized as described in Sec. A 2. The single and double dashed lines indicate the analytically calculated matching frequencies of the red and blue sideband transitions, respectively. These are based on the full (single-dashed) and RWA model (double-dashed). The cross marks indicate the numerically simulated results based on the full model. (a,b)  $f_q = 6.5$  GHz and  $f_c = 4.0$  GHz. (c,d)  $f_q = 4.0$  GHz and  $f_c = 6.5$  GHz.

- [2] Q. Xie *et al.* *The quantum Rabi model: solution and dynamics*, J. Phys. A **50**, 113001 (2017).
- [3] S. Felicetti *et al.* *Two-photon quantum Rabi model with superconducting circuits*, Phys. Rev. A **97**, 013851 (2018).
- [4] Y. Wang *et al.* *The mixed quantum Rabi model*, New J. Phys. **20**, 053061 (2018).
- [5] L. Duan *et al.* *The mixed quantum Rabi model*, Sci. Rep. **9**, 18353 (2019).
- [6] M. Hofheinz *et al.* *Generation of Fock states in a superconducting quantum circuit*, Nature **454**, 310 (2008).
- [7] F. Beaudoin *et al.* *First-order sidebands in circuit QED using qubit frequency modulation*, Phys. Rev. A **86**, 022305 (2012).
- [8] J. D. Strand *et al.* *First-order sideband transitions with flux-driven asymmetric transmon qubits*, Phys. Rev. B **87**, 220505(R) (2013).
- [9] B. Ann and G. A. Steele *Tunable and Weakly Invasive Probing of a Superconducting Resonator Based on Electromagnetically Induced Transparency*, Phys. Rev. A **102**, 053721 (2020).
- [10] B. Ann *et al.* *Sideband transitions in a two-mode Josephson circuit driven beyond the rotating-wave approximation*, Phys. Rev. Research. **3**, 033004 (2021)
- [11] D. A. Andrews *et al.* *Observation of Bloch-Siegert Shifts in the  $2^2S_{1/2}$ - $2^2P_{1/2}$  Microwave Resonance in Atomic Hydrogen*, J. Phys. B **8**, 1415 (1975).
- [12] T. Werlang *et al.* *Rabi model beyond the rotating-wave approximation: Generation of photons from vacuum through decoherence*, Phys. Rev. A **78**, 053805 (2008).

- [13] G. D. Fuchs *et al.* *Gigahertz Dynamics of a Strongly Driven Single Quantum Spin*, *Science* **326**, 5959 (2009).
- [14] J. Tuorila *et al.* *Stark Effect and Generalized Bloch-Siegert Shift in a Strongly Driven Two-Level System*, *Phys. Rev. Lett.* **105**, 257003 (2010).
- [15] I. Pietikäinen *et al.* *Observation of the Bloch-Siegert shift in a driven quantum-to-classical transition*, *Phys. Rev. B* **96**, 020501(R) (2017).
- [16] A. Blais *et al.* *Quantum-information Processing with Circuit Quantum Electrodynamics*, *Phys. Rev. A* **75**, 032329 (2007).
- [17] F. Deppe *et al.* *Two-photon probe of the Jaynes-Cummings model and symmetry breaking in circuit QED*, *Nat. Phys* **4**, 686 (2008)
- [18] S. Zeytinoglu *et al.* *Microwave-induced amplitude- and phase-tunable qubit-resonator coupling in circuit quantum electrodynamics*, *Phys. Rev. A* **91**, 043846 (2015)
- [19] Z. Chen *et al.* *Single-photon-driven high-order sideband transitions in an ultrastrongly coupled circuit quantum electrodynamics system*, *Phys. Rev. A* **96**, 012325 (2016)
- [20] S. Krinner *et al.* *Demonstration of an All-Microwave Controlled-Phase Gate between Far Detuned Qubits*, *Phys. Rev. Appl.* **14**, 044039 (2020)
- [21] J. R. Schrieffer and P. A. Wolff, *Relation Between the Anderson and Kondo Hamiltonians*, *Phys. Rev.* **149**, 491 (1966)
- [22] B. Ann (2021). Two-photon sideband transition in a driven quantum Rabi model : Quantitative discussions with derived longitudinal drives and beyond the rotating wave approximation. <https://doi.org/10.5281/zenodo.5149556>